

Exemplar-based inpainting as a solution to the missing wedge problem in electron tomography

Citation for published version (APA):

Trampert, P., Wang, W., Chen, D., Ravelli, R. B. G., Dahmen, T., Peters, P. J., Kubel, C., & Slusallek, P. (2018). Exemplar-based inpainting as a solution to the missing wedge problem in electron tomography. *Ultramicroscopy*, 191, 1-10. <https://doi.org/10.1016/j.ultramic.2018.04.001>

Document status and date:

Published: 01/08/2018

DOI:

[10.1016/j.ultramic.2018.04.001](https://doi.org/10.1016/j.ultramic.2018.04.001)

Document Version:

Publisher's PDF, also known as Version of record

Document license:

Taverne

Please check the document version of this publication:

- A submitted manuscript is the version of the article upon submission and before peer-review. There can be important differences between the submitted version and the official published version of record. People interested in the research are advised to contact the author for the final version of the publication, or visit the DOI to the publisher's website.
- The final author version and the galley proof are versions of the publication after peer review.
- The final published version features the final layout of the paper including the volume, issue and page numbers.

[Link to publication](#)

General rights

Copyright and moral rights for the publications made accessible in the public portal are retained by the authors and/or other copyright owners and it is a condition of accessing publications that users recognise and abide by the legal requirements associated with these rights.

- Users may download and print one copy of any publication from the public portal for the purpose of private study or research.
- You may not further distribute the material or use it for any profit-making activity or commercial gain
- You may freely distribute the URL identifying the publication in the public portal.

If the publication is distributed under the terms of Article 25fa of the Dutch Copyright Act, indicated by the "Taverne" license above, please follow below link for the End User Agreement:

www.umlib.nl/taverne-license

Take down policy

If you believe that this document breaches copyright please contact us at:

repository@maastrichtuniversity.nl

providing details and we will investigate your claim.



Exemplar-based inpainting as a solution to the missing wedge problem in electron tomography

Patrick Trampert^{a,b}, Wu Wang^{d,f}, Delei Chen^c, Raimond B.G. Ravelli^c, Tim Dahmen^{a,*}, Peter J. Peters^c, Christian Kübel^{d,e,g}, Philipp Slusallek^{a,b}

^a German Research Center for Artificial Intelligence GmbH (DFKI), 66123 Saarbrücken, Germany

^b Saarland Informatics Campus, 66123 Saarbrücken, Germany

^c The Institute of Nanoscopy, Maastricht University, 6211 LK Maastricht, The Netherlands

^d Institute of Nanotechnology, Karlsruhe Institute of Technology, Hermann-von-Helmholtz-Platz 1, 76344 Eggenstein-Leopoldshafen, Germany

^e Karlsruhe Nano Micro Facility, Karlsruhe Institute of Technology, Hermann-von-Helmholtz-Platz 1, 76344 Eggenstein-Leopoldshafen, Germany

^f Joint Research Laboratory Nanomaterials, Technische Universität Darmstadt, Jovanka-Bontschits-Straße 2, 64287 Darmstadt, Germany

^g Helmholtz-Institute Ulm for Electrochemical Energy Storage, Karlsruhe Institute of Technology, 89081 Ulm, Germany

ARTICLE INFO

Article history:

Received 8 April 2016

Revised 16 March 2018

Accepted 2 April 2018

Available online 21 April 2018

Keywords:

Missing wedge

Inpainting

Electron tomography

Tomographic reconstruction

Dictionary-based approaches

ABSTRACT

A new method for dealing with incomplete projection sets in electron tomography is proposed. The approach is inspired by exemplar-based inpainting techniques in image processing and heuristically generates data for missing projection directions. The method has been extended to work on three dimensional data. In general, electron tomography reconstructions suffer from elongation artifacts along the beam direction. These artifacts can be seen in the corresponding Fourier domain as a missing wedge. The new method synthetically generates projections for these missing directions with the help of a dictionary based approach that is able to convey both structure and texture at the same time. It constitutes a preprocessing step that can be combined with any tomographic reconstruction algorithm. The new algorithm was applied to phantom data, to a real electron tomography data set taken from a catalyst, as well as to a real dataset containing solely colloidal gold particles. Visually, the synthetic projections, reconstructions, and corresponding Fourier power spectra showed a decrease of the typical missing wedge artifacts. Quantitatively, the inpainting method is capable to reduce missing wedge artifacts and improves tomogram quality with respect to full width half maximum measurements.

© 2018 Published by Elsevier B.V.

1. Introduction

Electron tomography is one of the main methods for three-dimensional (3D) imaging at the nano-scale. It is extensively used both in structural biology and material science. The resolution is in the range of 1–20 nm, thereby filling a critical length scale gap for biological applications between atomic resolution of X-ray crystallography and single particle electron tomography [1] on the one hand, and high-resolution confocal light microscopy [2] and X-ray microscopy [3] on the other. In material science, the methods fill the gap between atom probe tomography [4] on the one side and Focused Ion Beam Scanning Electron Microscopy (FIB-SEM) [5] respectively X-ray Tomography techniques on the other.

In Electron tomography, projections from different directions are acquired by means of a transmission electron microscope and tilting the sample. A three-dimensional volume is numerically gen-

erated from these projections. Electron tomographic reconstructions often suffer from different restrictions, like opacity, limited field of view, limited number of projections, or missing wedge artifacts. A comprehensive review of computational methods involved in electron tomography studies with all these problems can be found in [6], and an evaluation of accuracy of several reconstruction algorithms with tubular objects as example was conducted in [7].

One of the most severe problems is the non-availability of projections covering the whole angular range. Most electron tomography datasets have a maximum angular range of about -75° – 75° , because of mechanical limitations of the specimen holder, shading of the area of interest by the support grid and the increasing projected thickness of the tilted specimen. This leads to elongation artifacts of reconstructed details along the symmetry center of projections. This is also visible in the Fourier domain as missing wedge, because no data is present in the angular range not imaged during data acquisition as predicted by the Fourier slice theorem [8]. This so called missing wedge problem introduces prominent

* Corresponding author.

E-mail address: Tim.Dahmen@dfki.de (T. Dahmen).

elongation artifacts along the beam direction of reconstructed objects [9] leading to an anisotropic spatial resolution [10].

2. Related work

Different approaches on tackling the missing wedge problem have been proposed, based mainly on (i) data collection, i.e. the way images are taken like using dual axis schemes, (ii) enabling a complete rotation of the specimen by using cylindrical samples geometries, and (iii) specialized reconstruction methods that address reconstructing missing information.

Changing the way of data acquisition by extending standard approaches of single axis tomography leads to better results regarding the missing wedge issue. Lee et al. [11] experimentally demonstrated, that equally sloped tomography (EST) can reduce missing wedge artifacts by constraining acquired images in a tilt series to have equally sloped angle increments. Another approach is double-tilt tomography, also called dual axis tomography (cf. [12,13]), where data is acquired from two perpendicular tilt axes. This technique reduces the missing wedge to a missing pyramid due to the fact that more information is present because of the two mutually perpendicular tilt series for one reconstruction. Dahmen et al. [14] proposed a combined tilt- and focal series as a new recording scheme for high-angle annular dark-field scanning transmission electron microscopy (STEM) tomography. Hereby, a tilt series with limited tilt range is supplemented by a through-focal series per tilt direction. The method results in a better sampling of the Fourier space and, thus, to a reduction of axial elongation artifacts.

Instead of using slab-like flat specimens for electron tomography, which restricts viewing angles, Kawase et al. [15] used a cylindrical specimen. The cylindrical shape allows imaging from a full range of viewing angles around the tilt axis, so that no missing wedge exists. They quantitatively analyzed the effect of the missing wedge on the volume fraction in a composite and the elongation due to the missing wedge. The work was extended by Kato et al. [16] who used rod-shaped specimens with different diameter for transmission electron tomography to evaluate the maximum usable rod diameter for the tomography specimen. While effective at avoiding the missing wedge problem altogether, the approach is not applicable in many situations, because manufacturing the rod-shaped specimen requires making a decision on the field of view prior to initial imaging and, thus, selecting the area of interest becomes difficult and the statistical sampling is limited. Furthermore, fabrication of such needle-shaped samples requires the material to be mechanically sufficiently strong, which is not the case for many materials.

Adapted reconstruction methods to handle missing information may also be capable of fighting the missing wedge. Baba et al. [17] performed a topographic analysis by stereo-photogrammetry to get pre-determined voxel arrangements for thin film-like replica-type specimens with some known properties. Using this prior knowledge as constraint in the reconstruction process reduces an infinite number of solutions due to the missing wedge to a finite number. Qualitatively enhanced reconstructions revealing fine structural parts showed no missing wedge effects. Zürner et al. [18] also used prior knowledge by adding a mask in each reconstruction step setting all voxels known to be vacuum in the samples to zero. A stronger assumption is made in the field known as discrete tomography. Hereby, the assumption is that the solution of the reconstruction problem has a sparse gradient, i.e. the sought tomogram consists of only a limited number of a priori known materials. The assumption obviously simplifies the problem and can be used to reduce missing wedge artifacts. A heuristic approach to discrete tomography is taken by the discrete algebraic reconstruction technique (DART) [19] and consecutive work. Another group of

algorithms based on the sparse gradient assumption are total variation minimization (TVM) techniques [20]. Contrary to DART, TVM techniques do not require the gray values to be known a priori, which can be an advantage for some applications.

Some algorithms that work without additional assumptions have also been reported to improve on missing wedge artifacts. A combination of the weighted back projection and SIRT, also called W-SIRT, claims an improved reconstruction with reduced elongated point spread in the direction of the missing tilt angles for a simple geometrical phantom, i.e. an improved reconstruction of spatial frequencies in the vicinity of the missing wedge [21]. The DIRECTT method (cf. [22,23]) is an iterative algorithm based on a sequence of alternating reconstructions and virtual projections of intermediate results, which are subsequently enhanced using residual sinograms instead of filtered back projections. DIRECTT reduces the typical missing wedge artifacts by variation of reconstruction parameters in the course of iterations.

In this study, we propose a heuristic method to estimate data from the missing projection directions using image processing techniques. The approach is orthogonal to reconstruction techniques that aim to generate better tomograms from incomplete data and could in principle be combined with any tomographic reconstruction algorithm.

3. Materials and methods

3.1. Inpainting algorithm

Our algorithm is inspired by the approach of Criminisi et al. [24]. The method originates from the field of image processing and was originally developed to fill missing regions in photographs in a way that this is not perceivable for the human eye after using the so called exemplar-based inpainting. Based on the surroundings, a hole is filled step by step by inserting small parts of the known image regions, called patches.

We found that the capability of the method to replicate both texture and structure can also be utilized to generate data for the missing tilt angle range. This seemingly surprising result can intuitively be understood from the fact that sinograms generated from a tilt series consist of the superposition of continuous curves. A reasonable guess on how the data in the missing wedge looks like should respect continuity, particularly in the angular dimension. Additionally, many samples exhibit some degree of local self-similarity. In the absence of additional data, continuing structures with patterns observed elsewhere in the sinogram, thus, results in better estimates than statistical methods, such as filling in the average gray value or using random distributions of gray values, are able to achieve. The method generates data in the missing wedge by computing the most likely continuation of the sinogram under the assumption that tilt series are both continuous and to some degree redundant.

A pseudo-code of the algorithm (Fig. 1) give a summary of the inpainting algorithm for 3D ET data.

In many cases, the TEM sample and respectively the ET data has an approximately slab-like geometry, which means that the thickness of a specimen as seen by the electron beam differs with the tilt angle. As the missing wedge inpainting assumes a cylindrical geometry, ET data has to be normalized in a preprocessing step. By dividing each projection through its mean intensity, the original geometry is mapped to a cylindrical geometry with uniform distances. Hereby, the imaging mode has to be considered. In HAADF-STEM, the intensity is proportional to the sample thickness, so the simple division should work. In BF-TEM the intensity is proportional to the log of the sample thickness and would have to be linearized prior to the division. The normalized data is then used as input for the inpainting algorithm.

Algorithm 3D Missing Wedge Inpainting
Input ET image stack S , patch size ψ
begin
 1: normalize S to comply with a cylindric geometry
 2: extend S with empty projections
 3: extract fillfront F
 4: **while** ($F \neq \emptyset$)
 5: compute priorities $P(v) \forall v \in F$
 6: identify $v' = \operatorname{argmax}_v P(v)$
 7: find $w \in \Omega$ that minimizes $K(c)$
 8: copy image data from Ψ_w to $\Psi_{v'}$, $\forall v \in \Psi_{v'} \cap \Omega$
 9: update $P(v) \forall v \in \Psi_{v'}$
 10: **end while**
end
Output extended ET image stack that covers full tilt range

Fig. 1. Pseudo-code for the inpainting procedure for 3D ET data.

Having acquired an ET image stack, projections are added to this stack, so that each missing tilt angle is initialized with an empty projection. All empty projections together constitute the target volume Ω that will be filled during the inpainting procedure. The acquired projections that are available as prior knowledge constitute the source volume Φ . An additional mask is given as input to tell the algorithms which voxels belong to source and which ones to target.

The inpainting is an iterative process that inserts small image parts of the source volume, called patches, into the target volume. A template window $\psi = \psi_x \times \psi_y \times \psi_z$ has to be specified as size for this patch. ψ is highly dependent on the dataset to be inpainted. In practice ψ has to be set a little larger than the largest distinguishable texture element in the source volume. We have set ψ to $9 \times 9 \times 9$ as default window, but also evaluated different window sizes for a chosen particle dataset. Each patch is centered at a voxel v , which will be used as patch identifier ψ_v from now on.

The order of filling is crucial as texture and structure should be propagated from source volume to target volume. Hence, patches that are on the continuation of strong edges and additionally are surrounded by high-confidence voxels must be filled first. This means a prioritization order for filling patches must be determined. Each source volume voxel v that is a direct neighbor of a target volume voxel is a possible candidate and gets assigned to the so called fillfront. The for this purpose computed priority $P(v)$ consists of a confidence term $C(v)$ and a data term $D(v)$.

The computation of the confidence $C(v)$ of voxel v works as follows:

$$C_{init}(v) = \begin{cases} 0, & \text{if } v \in \Omega \\ 1, & \text{if } v \in \Phi \end{cases}, \quad C(v) = \frac{\sum_{q \in \Psi_v \cap \text{source}} C(q)}{|\Psi_v|}$$

where Ψ_v is the patch centered at voxel v , q are all voxels in the intersection of a patch and the source region, and $|\Psi_v|$ is the number of voxels of the patch.

The data term $D(v)$ of voxel v is computed by

$$D(v) = \frac{|\nabla I_v^\perp \cdot n_v|}{I_{max}}$$

where ∇I_v^\perp is the isophote at voxel v of Image I , that means orthogonal (\perp) to the gradient ∇ , n_v is a unit vector orthogonal to the fillfront in voxel v , and I_{max} is the dynamic range of the voxel

values, which is the biggest possible gray value in an image, i.e. $2^{\#bits} - 1$, e.g. for 8 bit images it is 255.

Having computed confidence term and data term the priority value $P(v)$ of a voxel v is computed by

$$P(v) = \begin{cases} C(v) \cdot D(v), & \text{if } D(v) > 0 \\ C(v), & \text{if } D(v) = 0 \end{cases}$$

In each iteration the maximal value $v' = \operatorname{argmax}_v P(v)$ determines the position where the next patch is inserted. $\psi_{v'}$ is then compared to every patch that completely fits into the source region by computing a similarity measure between both. We extended the originally proposed sum of squared differences (SSD) to a kernel based similarity measure.

Inspired from Kernel Learning in Machine Learning, we used the well-known radial basis function (RBF) kernel [25] to define a similarity measure, which is defined as

$$K(P_t, P_s) = \exp\left(-\frac{\|P_t - P_s\|^2}{2 \cdot I_{max}}\right), \quad \|P_t - P_s\|^2 = \sum_{\substack{i=1 \\ t \in P_t, s \in P_s}}^{|\Psi_v|} (t_i - s_i)^2$$

where P_t is the target patch, i.e. the patch where data will be inserted, and P_s is a source patch, i.e. a candidate patch whose voxels will be inserted where P_t has no values yet. $K \in (0, 1]$ with 0 meaning no similarity and 1 meaning the patches are identical.

As P_t consists of known voxels from the source region as well as voxels with no information, it is not straightforward to compute a similarity measure between P_t and a candidate patch. Furthermore, voxels that have no value yet must not be ignored in the similarity computation, because doing so can lead to the introduction of artifacts during inpainting that can propagate further (see Fig. 2), which may severely influence the resulting inpainting. As a solution, we introduce a new similarity measure that penalizes patches where the unknown data deviates from the mean of the known data, thus avoiding the introduction of high contrast features (see also Fig. 2b) unless supported by data.

The new similarity measure consists of two parts: (i) a RBF Kernel $K_1(P_{t|known}, P_s)$ for the part of the input patch where data is available denoted as $P_{t|known}$, and (ii) a RBF Kernel $K_2(\mu_{t|known}, P_s)$ for the part of the input patch that has no information yet, where

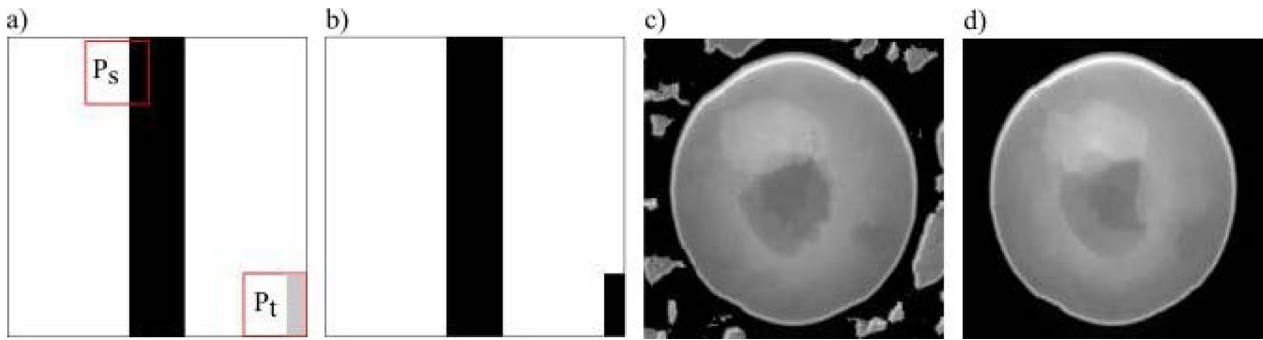


Fig. 2. Example of the possible introduction of artifacts when ignoring the target region in the similarity measure. (a) P_t is the patch where data should be inserted; here white and black areas are already filled and the gray area has no values yet. The patch P_s is a possible candidate for the insertion when leaving out voxels that have no value yet in the similarity computation. (b) This leads to the introduction of an artifact. As example an inpainted Shepp-Logan phantom projection is shown. (c) Result using $K(1)$ with ignored target region, which has introduced many artifacts. (d) Result using $K(0.999)$.

$\mu_{t|known}$ is the mean value of the known input patch voxels. K_1 and K_2 are then combined as convex combination

$$K(c) = c \cdot K_1 + (1 - c) \cdot K_2$$

with $c \in [0, 1]$ resulting in $K_c \in [0, 1]$, which is still a kernel function [25]. We have set c to 0.999, as conducted experiments showed that a small contribution from K_2 is enough to prevent the occurrence of artifacts like in Fig. 2.

The candidate patch with maximal K_c constitutes the most similar patch P_{best} . Every voxel of P_t that has no information yet is then replaced by the corresponding voxel of P_{best} .

At the end of each iteration the fillfront has to be updated, which means voxels that were inpainted are deleted and voxels that are adjacent to the inserted patch are added. Different from the original approach, new priority values are computed for each voxel of the fillfront that was affected by the inserted patch. Instead of freezing already computed confidence values, we changed the computation of the confidence. Added voxels are assigned a confidence value $C_{adaptive}(V_{new}) = \frac{1}{\#iterations}$. Afterwards, each affected voxel is recomputed. This ensures that the target region is inpainted slice by slice, which stabilizes the whole inpainting process. Having updated the priority values, the next patch to be inserted can be computed. This is done until there are no voxels left in the fillfront and the whole volume has been filled. The final inpainted projections can then be used with any reconstruction algorithm to compute a reconstructed volume.

3.2. Own contributions

Apart from the idea of applying exemplar based inpainting to the missing wedge problem, our contributions are as follows: (1) We limited our method to the inpainting of gray values. (2) The original algorithm only works on two dimensional (2D) data. We extended the ideas to work on three-dimensional data, such as ET tilt series. That means, we extended the 2D method to work on 3D data using 3D patches, which has not been done yet to the best of our knowledge. (3) We replaced the L_2 -norm used as similarity measure in the original algorithm by the RBF kernel. (4) We introduced the new confidence value $C_{adaptive}$ as explained above.

3.3. Implementation

The new method is computationally very demanding on 3D data. During one iteration, many similarity measure computations for voxels, respectively patches, have to be computed by the algorithm. As this task is highly parallelizable and most performance critical in the method, we implemented this part on graphics processing unit (GPU) via OpenCL [26]. Furthermore, we minimized

the amount of data that has to be transferred from central processing unit (CPU) to GPU and vice versa, as bandwidth plays a crucial role in GPU programming.

3.4. Datasets used for evaluation

For the evaluation of our approach we used datasets of size $256 \times 256 \times N$ and $450 \times 450 \times N$, where N is the number of projections. The datasets were (i) the well-known Shepp-Logan phantom [27], which is a standard synthetic test dataset for reconstruction algorithms, (ii) a downsized catalyst dataset, and (iii) a dataset containing colloidal gold particles. The artificial dataset is well suited to compare parameters and reconstruction conditions more easily and with higher validity, whereas the real datasets are used for judging the algorithms capabilities under real conditions.

The 3D Shepp-Logan phantom was created using Matlab and ground truth data was generated for the angular range of $\pm 90^\circ$. All projections of $\pm 90^\circ$ in 1° steps constitute the ground truth dataset, and the projections of $\pm 62^\circ$ were used as input for the inpainting and constitute the incomplete data. All projections from -90° to -63° and from 63° to 90° were used for the comparison of generated projections and ground truth projections.

The second dataset was a catalyst dataset. The powder of the 1 wt.% Au/TiO₂ catalyst was directly dispersed on copper grid with carbon support film. Electron tomography was performed using an Titan 80–300 microscopy (FEI) operated at an acceleration voltage of 300 kV in STEM mode. The 2048×2048 pixels STEM images with a pixel size of 0.23 nm were collected with a high-angle annular dark-field detector using the Xplore3D software over a tilt range of $\pm 76^\circ$ with a tilt increment of 1° . Alignment of the tilt series was performed using IMOD with the Au nanoparticles as fiducial markers resulting in a residual mean error for the alignment of 0.8 pixel. The aligned projections were downsized to 450×450 pixels resolution to compensate for long runtimes of the algorithm.

For the third dataset, colloidal gold particles with a diameter of 15 nm were applied from aqueous suspension to a TEM carbon coated copper grid, followed by drying in air. Tomography was performed in bright-field TEM electron microscope, operated at 120 kV. A tilt series was acquired over a tilt range from -70° to 68° with step increment of 1° and a defocus of $-5 \mu\text{m}$, using the TOMO4 software (FEI, Eindhoven). The nominal magnification was 23,000 corresponding to a pixel size of 0.48 nm. The alignment of the tilt series was performed in IMOD [28] based on fiducial markers. The aligned tilt series was binned to 0.96 nm (binning factor 2) and then a region of interest of 256×256 was cropped for our study.

3.5. Evaluation metrics

Several evaluation metrics that address comparability of ground truth data and estimated data, which can be projections or reconstructions, were used in this study. Standard evaluation metrics we applied were the root mean squared error (RMSE) [29], the Peak signal-to-noise ratio (PSNR) [30] and the structural similarity index (SSIM) [31]. Furthermore, we used the FWHM to show an increase in resolution of inpainted reconstructions compared to incomplete reconstructions.

For assessing reconstruction quality on real data we estimated the resolution with help of the full width half maximum (FWHM) of the point spread function at different positions in the reconstructed volume, because FWHM is a good approximation of the possible resolution [14]. Line profiles were measured for all particles in the reconstructed dataset. The width at half the maximum was linearly interpolated based on enclosing voxels, which was needed due to discrete data.

4. Results

For the evaluation of our algorithm we compared (i) inpainted projections with ground truth projections, (ii) reconstructions of hybrid data, which is the original data with added inpainted projections, and ground truth data, (iii) reconstructions of hybrid data and incomplete data, (iv) the Fourier power spectra of reconstructions of hybrid data and ground truth data, and (v) the Fourier power spectra of reconstructions of hybrid data and incomplete data. Missing wedge effects are clearly visible in the Fourier power spectrum, which makes it a great visual indicator for the applicability of our new method.

We applied the developed algorithm with a fixed patch size of $\psi = 9 \times 9 \times 9$ to the Shepp-Logan phantom dataset and to the catalyst dataset. Reconstructions were performed with the software package Ettention [32] using simultaneous iterative reconstruction technique (SIRT) with 300 iterations. The algorithm and iteration choice was inspired by [21]. Outcomes were evaluated on the basis of the introduced evaluation metrics as well as visual inspection of inpainted projections, reconstructions in xy -direction, resliced reconstructions in xz -direction, and the corresponding Fourier power spectra. Furthermore, we applied the algorithm to the gold particle dataset with varying patch sizes from $\psi = 5 \times 5 \times 3$ to $\psi = 21 \times 21 \times 21$. We only compared sinograms of inpainted projections visually to show how particle size and corresponding choice of ψ influence the inpainting algorithm.

4.1. Shepp-Logan phantom

We compared a Shepp-Logan phantom reconstructed from the full tilt range (Fig. 3a) with one reconstructed from hybrid data (Fig. 3b) and one reconstructed from incomplete data (Fig. 3c).

Fig. 4 shows selected inpainted projections from -63° to -90° . The further away the inpainted projections were from the input of range of $\pm 62^\circ$, the more the inpainted projections deviated from the real ones. Nevertheless, even the projection at -90° showed visual similarity to Shepp-Logan phantom projections. Projections in the upper tilt angle range between 63° and 90° behaved analogously.

Taking the evaluation metrics confirmed the visual inspection results. SSIM and PSNR of the 56 inpainted projections were 0.75 ± 0.1 and 30.91 ± 5.54 . Looking at reconstructions reinforced the first impressions from the results of inpainted projections (Fig. 5). The xy -direction of reconstructions of ground truth data, hybrid data, and incomplete data are shown in Fig. 5a–c. The reconstruction with incomplete data showed clear artifacts coming from the missing wedge. The round shape of the phantom was

deformed in the missing wedge area. There were also artifacts in the area around the phantom (Fig. 5f). In the reconstruction from hybrid data (Fig. 5e) there were hardly any artifacts left from the missing wedge. However, the interior of the phantom shows a new type of artifact, expressed as smearing. A PSNR of 35.53 for the reconstruction from hybrid data confirmed the good quality compared to the incomplete data reconstruction with a PSNR of 18.76. SSIM was higher for the hybrid data reconstruction with 0.9833 than for the incomplete data reconstruction with 0.7624. RMSE was reduced by a factor of around 14. Finally, the Fourier power spectrum of the incomplete data (Fig. 5i), which reflects the missing data by a missing wedge, was completely filled, as can be seen in Fig. 5g–h. For the Fourier power spectra of the hybrid data reconstruction and the ground truth data reconstruction we acquired a PSNR of 44.36 and a SSIM of 0.9611.

4.2. Catalyst data

The catalyst data had only projections in the range of $\pm 76^\circ$ due to the approximate slab-geometry or because of mechanical limitations of the specimen holder and supporting copper grid. From these data, we selected a range of projections from $\pm 62^\circ$ to make the dataset comparable to our other experiments. As there is no ground truth we measured FWHM of each particle in the reconstructed datasets to compare resolution. The compared datasets were (i) the reconstruction of the original data with a tilt range of $\pm 62^\circ$ (MW) and (ii) the inpainted data, which constitutes a tilt range of $\pm 90^\circ$ (EBI) (Fig. 6).

The dataset contained 25 particles that were used to measure FWHM in the reconstructions in xz -direction. The original data reconstructions FWHM was 11.2 ± 3.5 pixels, whereas the inpainted data reconstructions FWHM was 9.9 ± 2.6 pixels. To ensure that the result is statistically significant, a paired two-tailed t -test was conducted, which resulted in a p -value of $3 \cdot 10^{-5}$. Two particles and the corresponding line profiles are depicted in Fig. 7. Additionally, we conducted a size analysis of the particles in 2D based on the 0° projection. The average particle size was 8.8 ± 2.6 pixels, which shows that the smaller particle sizes of the hybrid data reconstructions are closer to the real sizes.

4.3. Colloidal gold particles

Furthermore, we acquired a real dataset of gold particles and evaluated the inpainting algorithm with different patch sizes $\psi_x \times \psi_y \times \psi_z$. We handpicked different worst-case situations with particularly string artifacts (Fig. 8) to show that results were heavily influenced by the used patch size. One black curve constitutes the movement of one gold particle during tilting in the sinogram. The structures in between the two horizontal black lines in each sinogram constitute the original data. Above and below the black lines is the inpainted data. We observed different behaviors of the inpainting algorithm when looking at varying patch sizes and individual gold particles. For curves with low curvature, the inpainting continued the curves (Fig. 8a–e). For all these examples ψ_z was at least 15, whereas ψ_x and ψ_y varied a lot. This means the patch size in z -directions plays an important role and must be chosen at least as large as the particles in the projections. Fig. 8f–h are examples for a too small choice of ψ_z . For particles that resemble a high curvature in the sinogram (Fig. 8i–p) the inpainting algorithm has problems. These problems ranged from unreasonable continuation of a curve at one (Fig. 8j) or both boundaries (Fig. 8l) of the range to stopping or no continuation of a curve (Fig. 8p) as well as introduction of artifacts (Fig. 8o). The presented approach mainly aims at recovering linear structures, that means the higher the curvature of an object is, the less likely it is that the algorithm

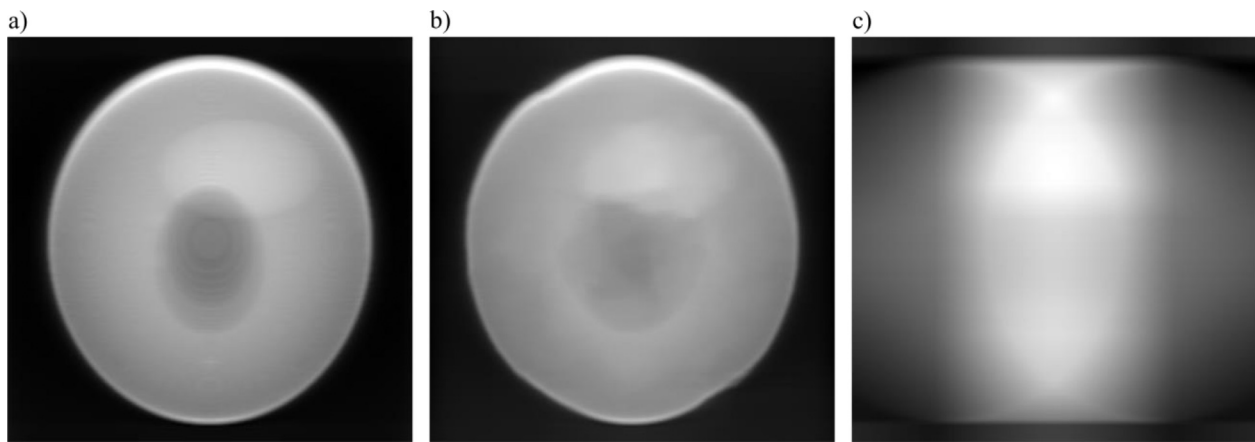


Fig. 3. (a) Shepp-Logan phantom, reconstructed from the full tilt range. (b) Shepp-Logan phantom, reconstructed from hybrid data. (c) Shepp-Logan phantom, reconstructed from incomplete data (tilt range of $\pm 62^\circ$). For all cases, the image shows the projection at -90° .

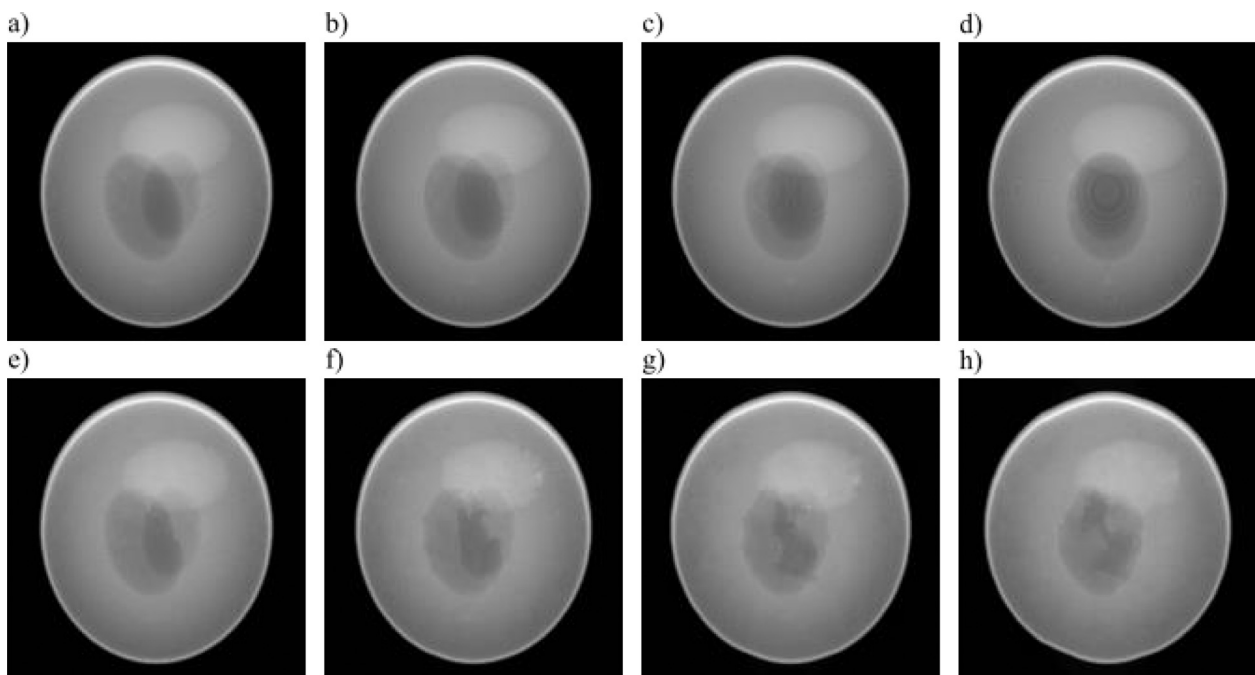


Fig. 4. Comparison of several projections between ground truth data (upper row) and inpainted data (lower row) of Shepp-Logan phantom. From left to right projections with tilt angles -63° , -70° , -78° , and -90° are depicted.

works. Hence, the left curve in Fig. 8m–p was never recovered, no matter how the patch size had been chosen.

5. Discussion

We developed a new method to reduce missing wedge artifacts and evaluated it on several datasets. The evaluation was conducted as visual comparison of projections and reconstructions as well as by taking several evaluation metrics for judging the quality of the results quantitatively.

The Shepp-Logan phantom served as an artificial ground truth dataset to be able to assess the performance of the inpainting algorithm. The inpainted projections continued the tilt series reasonably. This was also confirmed by the enhanced reconstruction results, both visually and by means of the evaluation metrics. The algorithm enhanced structure identification of the ellipses that comprise the phantom. However, there were also new artifacts in the hybrid data reconstruction, which could be seen as smearings inside the phantom. This is a concern, as the structure of typical

missing wedge artifacts is familiar to most tomography users and can easily be recognized as such. The introduction of new, per se unfamiliar artifacts introduces the risk of mistaking them for structures inside the sample. The newly introduced artifacts are much less pronounced than the typical missing wedge artifacts and thus can be acceptable or not depending on the application. For example, in many biological samples the inpainting artifacts pose a risk for misinterpretation. Contrary, in material science samples where the primary interest is the morphology of a microstructure, the typical missing wedge artifacts hide crucial questions, such as the connection or separation of phase grains.

While experimenting with the Shepp-Logan phantom data, it also showed that the new method became less advantageous, when the input dataset had only few projections. Such datasets are acquired when tilt angle steps are quite big, e.g. 3° steps or even more, or when the tilt angle range is very small, e.g. from -30° to 30° . Therefore, this kind of data cannot provide enough information, respectively a big enough source region. Furthermore, big tilt increments lead to gaps between two projections that falsify

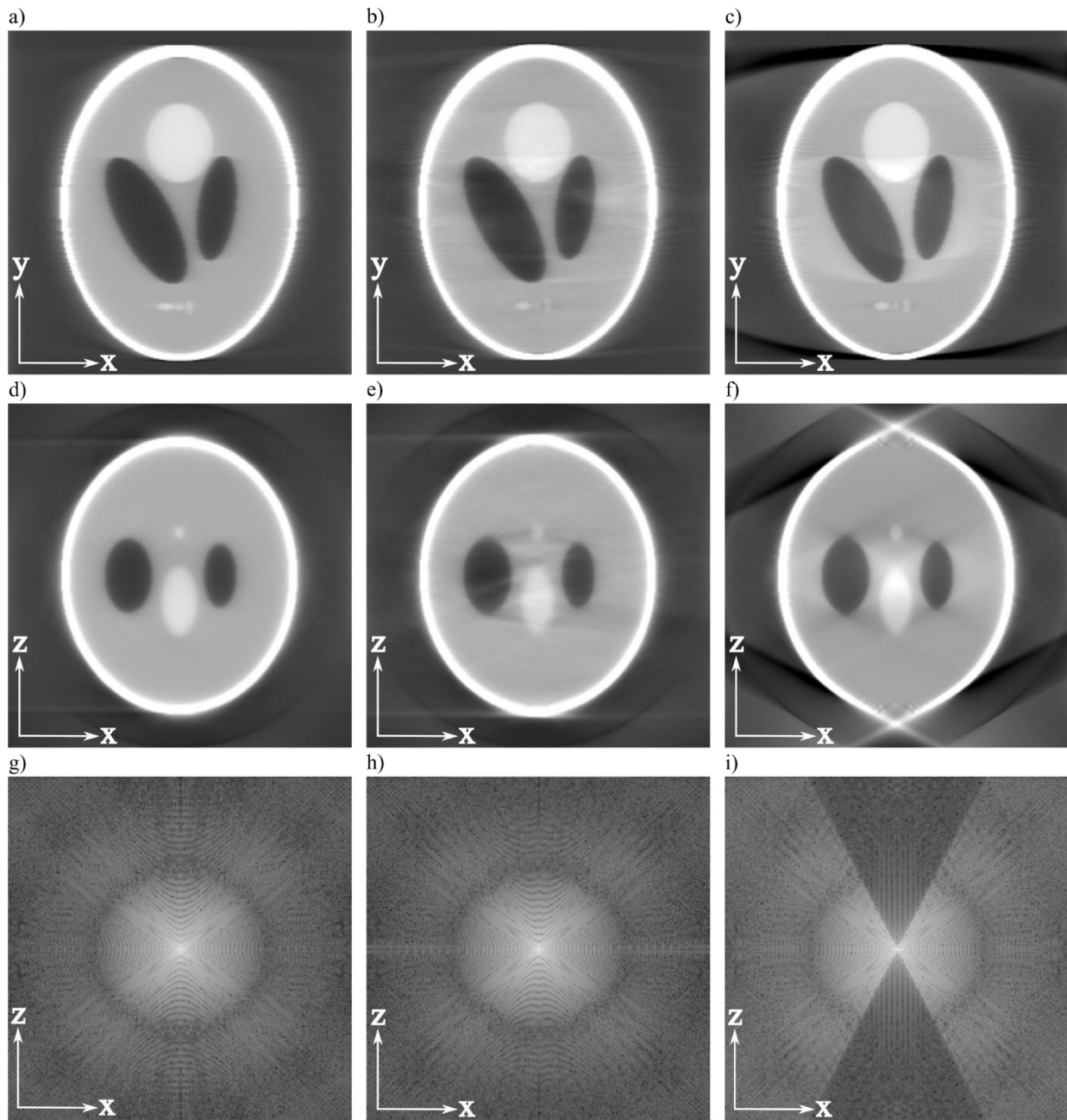


Fig. 5. Comparison of reconstruction results of Shepp-Logan phantom. From left to right: (a,d,g) Reconstruction from ground truth data. (b,e,h) Reconstruction from hybrid data. (c,f,i) Reconstruction from incomplete data. The upper row shows slice 128 of the reconstructed volume in xy-direction. The middle row shows slice 64 of the resliced volume in xz-direction. The lower row shows the corresponding Fourier power spectrum of slice 112 in xz-direction.

neighborhood relationships, which impedes a meaningful inpainting. In such situations the new method should not be applied as it is, because it brings no benefits.

Applying the new method to a real catalyst dataset supported the positive results of the Shepp-Logan phantom. The catalyst dataset contained 25 particles whose resolution was enhanced by applying the inpainting procedure as preprocessing to the reconstruction. This was both visible when comparing the reconstruction results and confirmed by the significantly reduced FWHM values for the hybrid data reconstruction. The shape of the particles was ellipsoidal in the incomplete data reconstructions, whereas the particles in the hybrid data reconstruction appeared spherical, which shows that elongation artifacts caused by the missing data were significantly reduced due to the inpainting procedure. Even

small particles gained resolution, which facilitated detection. Furthermore, we could not identify new artifacts as for example the smearings in the Shepp-Logan phantom.

An exploration of the parameter space, which means different patch sizes, was conducted to give further insights on improvements of the method. In general, the patch size should be at least as large as the size of the features in question. Recovered areas of the gold particle dataset seemed to depend on the patch size, i.e. even in the same dataset, different areas achieved best results with different patch sizes. Looking further into that could be utilized to improve the method. Adaptive algorithms that work on the basis of a local neighborhood might be of advantage. Extending the inpainting algorithm so that it becomes specialized for electron microscopy data in the sense that the sinusoidal movement of indi-

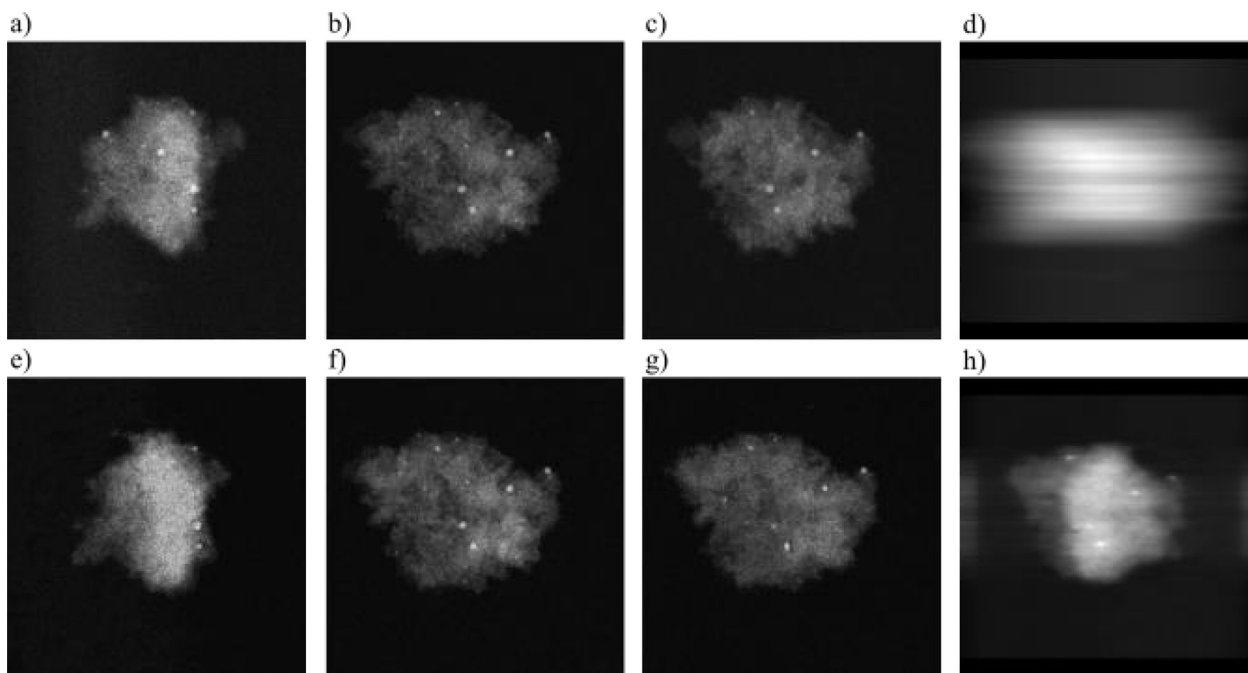


Fig. 6. Comparison of several projections between ground truth (upper row) and hybrid (lower row) catalyst data. From left to right projections with tilt angle 76° , -63° , -70° , and -90° are depicted. The -90° projections were acquired from a virtual projection of the reconstructed data.

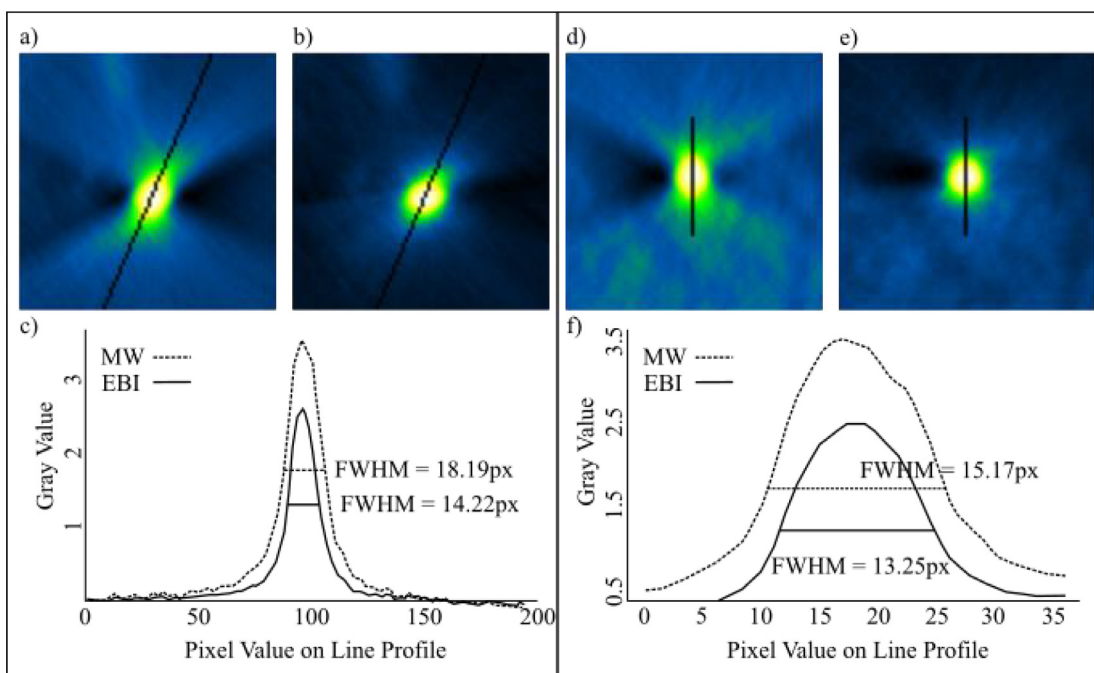


Fig. 7. Particle comparison and corresponding line profiles with FWHM values. (a) and (d) are two particles in xz -direction that were reconstructed with the original dataset ranging from -62° to 62° depicted as MW. (b) and (e) are the corresponding particles reconstructed with the inpainted dataset depicted as EBI. (c) shows the line profile of the particles from (a) and (b), and (f) shows the line profiles of the particles from (d) and (e). FWHM values are much smaller for the inpainted reconstructions.

vidual particles in the projections, as seen in a sinogram, is taken into consideration could also enhance results when used as prior for salient structure completions.

The experiments also showed that runtime is an issue that has to be tackled. On an AMD Radeon R9 390, the method took around 90 min on $256 \times 256 \times 181$ resolution datasets, where 56 projections of size 256×256 had to be inpainted. Further experiments showed, that it scaled quadratically with increasing resolution. In addition to implementing the main parts of the algorithm on GPU,

there is much potential for further improvements towards shorter execution times. Preliminary results indicate that the issue can alternatively be addressed with the introduction of novel acceleration structures for exemplar-based inpainting [33].

In the performed experiments, inpainted and real projections complemented each other reasonably. Also the evaluation metrics showed the gain of the method based on artificial and real datasets. For the Shepp-Logan phantom, visual results already sufficed to see that the new method has a positive effect. For the cat-

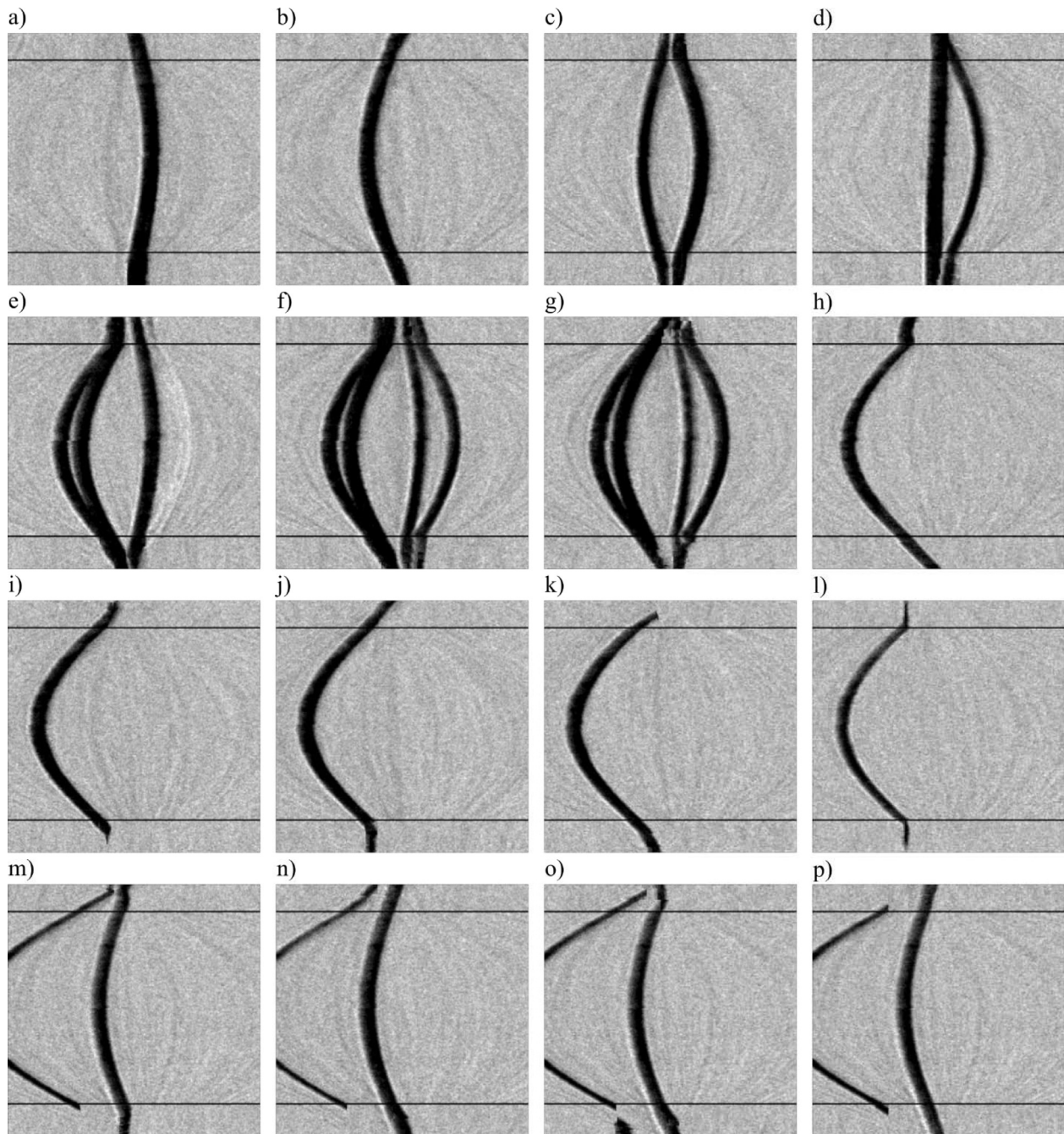


Fig. 8. Effect of the selection of the patch size parameters on the inpainting results. Hybrid data is situated above and below the black horizontal lines generated with projections from -70° to 68° , which is depicted in between the black horizontal lines. (a) slice 103, $\psi = 7 \times 7 \times 15$, (b) slice 216, $\psi = 13 \times 13 \times 19$, (c) slice 132, $\psi = 5 \times 5 \times 21$, (d) slice 47, $\psi = 13 \times 13 \times 15$, (e) slice 72, $\psi = 9 \times 9 \times 15$, (f) slice 67, $\psi = 11 \times 11 \times 11$, (g) slice 66, $\psi = 15 \times 15 \times 9$, (h) slice 174, $\psi = 19 \times 19 \times 9$, (i) slice 243, $\psi = 9 \times 9 \times 11$, (j) slice 246, $\psi = 13 \times 13 \times 21$, (k) slice 248, $\psi = 19 \times 19 \times 9$, (l) slice 251, $\psi = 7 \times 7 \times 7$, (m) slice 224, $\psi = 19 \times 19 \times 9$, (n) slice 223, $\psi = 17 \times 17 \times 21$, (o) slice 224, $\psi = 19 \times 19 \times 15$, and (p) slice 224, $\psi = 11 \times 11 \times 21$.

alyst data, comparing the reconstructions of the particles visually as well as with FWHM unveiled the positive impact on a material science dataset. This may be an ideal use case for our method, where the focus lies in analyzing contained particles. The parameter space exploration further showed that there is a lot of potential to enhance performance for such kind of data.

6. Conclusion

We have presented a new algorithmic approach to reduce missing wedge artifacts. Inspired by exemplar-based inpainting in im-

age processing, we contrived a new algorithm that is capable to heuristically generate appropriate data for the missing wedge. The method acts as preprocessing before a subsequent tomographic reconstruction and adds further projections to the original input data. Integrating these into a reconstruction enhances results by reducing the missing wedge, which leads to fewer artifacts in the final reconstruction. Furthermore, elongation artifacts in xz -direction are reduced, which enhances resolution.

Performance issues and the possible introduction of new artifacts are the main concerns of the new method. Regarding performance, we are optimistic that this can be fixed by techni-

cal improvements. Regarding the artifacts, the method must be used keeping this drawback in mind. An additional comparison with original reconstructions may help to prevent wrong conclusion due to introduced artifacts. As soon as runtime performance has reached an acceptable level for daily application, the missing wedge inpainting may become an important preprocessing step before subsequent reconstructions of material science tasks that involve limited angle electron tomography. Currently, considering the conducted experiments, the new method works well for datasets with small equidistant tilt angle steps of around 1° and a range that includes at least the range from -60° to 60° . Further research has to be performed to improve runtime performance on bigger datasets and to get a better understanding of exemplar-based inpainting for solving the missing wedge problem.

Acknowledgement

Research has been funded within the European Research Project NOTOX (FP7-267038). The authors thank the DFKI GmbH for additional funding and for providing the necessary infrastructure. Furthermore, we thank Ghazal Tofighi (Institute for Chemical Technology and Polymer Chemistry, Karlsruhe Institute of Technology) for synthesizing and providing Au/TiO₂ catalyst.

References

- [1] J. Frank, *Three-Dimensional Electron Microscopy of Macromolecular Assemblies*, Oxford University Press, 1996.
- [2] S.W. Hell, Far-field optical nanoscopy, *Science* 316 (May (5828)) (2007) 1153–1158.
- [3] W. Meyer-Ilse, D. Hamamoto, A. Nair, S.A. Lelièvre, G. Denbeaux, L. Johnson, A.L. Pearson, D. Yager, M.A. Legros, C.A. Larabell, High resolution protein localization using soft X-ray microscopy, *J. Microsc.* 201 (no. Pt 3. March) (2001) 395–403.
- [4] T.F. Kelly, M.K. Miller, Invited review article: atom probe tomography, *Rev. Sci. Instrum.* 78 (3) (2007) 1–20.
- [5] M. Cantoni, L. Holzer, Advances in 3D focused ion beam tomography, *Mrs Bull* (2014).
- [6] J.J. Fernandez, Computational methods for electron tomography, *Micron* 43 (10) (2012) 1010–1030.
- [7] D. Chen, B. Goris, F. Bleichrodt, H.H. Mezerji, S. Bals, K.J. Batenburg, G. de With, H. Friedrich, The properties of SIRT, TVM, and DART for 3D imaging of tubular domains in nanocomposite thin-films and sections, *Ultramicroscopy* 147 (2014) 137–148.
- [8] S. Zhao, H. Halling, A new Fourier method for fan beam reconstruction, *Nucl. Sci. Symp. Med.* (0) (1995) 1287–1291.
- [9] N. Kawase, M. Kato, H. Nishioka, H. Jinnai, Transmission electron microtomography without the 'missing wedge' for quantitative structural analysis, *Ultramicroscopy* 107 (1) (2007) 8–15.
- [10] M. Radermacher, Three-dimensional reconstruction of single particles from random and nonrandom tilt series, *J. Electron Microsc. Tech.* 9 (4) (1988) 359–394.
- [11] E. Lee, B.P. Fahimian, C.V. Iancu, C. Suloway, G.E. Murphy, E.R. Wright, D. Castaño-Díez, G.J. Jensen, J. Miao, Radiation dose reduction and image enhancement in biological imaging through equally-sloped tomography, *J. Struct. Biol.* 164 (November (2)) (2008) 221–227.
- [12] P. Penczek, M. Marko, K. Buttle, J. Frank, Double-tilt electron tomography, *Ultramicroscopy* 60 (October (3)) (1995) 393–410.
- [13] I. Arslan, J.R. Tong, and P.A. Midgley, "Reducing the missing wedge: High-resolution dual axis tomography of inorganic materials," vol. 106, pp. 994–1000, 2006.
- [14] T. Dahmen, J.-P. Baudoin, A.R. Lupini, C. Kübel, P. Slusallek, N. de Jonge, Combined scanning transmission electron microscopy tilt- and focal series, *Microsc. Microanal.* 20 (April (2)) (2014) 548–560.
- [15] N. Kawase, M. Kato, H. Nishioka, H. Jinnai, Transmission electron microtomography without the 'missing wedge' for quantitative structural analysis, *Ultramicroscopy* 107 (January (1)) (2007) 8–15.
- [16] M. Kato, N. Kawase, T. Kaneko, S. Toh, S. Matsumura, H. Jinnai, Maximum diameter of the rod-shaped specimen for transmission electron microtomography without the 'missing wedge', *Ultramicroscopy* 108 (3) (2008) 221–229.
- [17] N. Baba, E. Katayama, A novel 'ghost'-free tomographic image reconstruction method applicable to rotary-shadowed replica specimens, *Ultramicroscopy* 108 (3) (2008) 239–255.
- [18] A. Zürner, M. Döblinger, V. Cauda, R. Wei, T. Bein, Discrete tomography of demanding samples based on a modified SIRT algorithm, *Ultramicroscopy* 115 (2012) 41–49.
- [19] K. Batenburg, J. Sijbers, DART: a fast heuristic algebraic reconstruction algorithm for discrete tomography, *Image Process. 2007. ICIP 2007.*, 4(2), 2007 IV–133.
- [20] B. Goris, W. Van den Broek, K.J. Batenburg, H. Heidari Mezerji, S. Bals, Electron tomography based on a total variation minimization reconstruction technique, *Ultramicroscopy* 113 (February) (2012) 120–130.
- [21] D. Wolf, A. Lubk, H. Lichte, Weighted simultaneous iterative reconstruction technique for single-axis tomography, *Ultramicroscopy* 136 (2014) 15–25.
- [22] A. Kupsch, A. Lange, Reconstruction of Limited View Tomography Data by DIRECTT, in: *Proc. 18th World*, 2012, pp. 16–20. no. April.
- [23] A. Kupsch, A. Lange, M.P. Hentschel, S. Lück, V. Schmidt, R. Grothausmann, A. Hilger, I. Manke, Missing wedge computed tomography by iterative algorithm DIRECTT, *J. Microsc.* (2015).
- [24] A. Criminisi, P. Pérez, K. Toyama, Region filling and object removal by exemplar-based image inpainting, *IEEE Trans. Image Process.* 13 (9) (2004) 1200–1212.
- [25] T. Hastie, R. Tibshirani, J. Friedman, *The Elements of Statistical Learning*, 2001.
- [26] J.E. Stone, D. Gohara, G. Shi, OpenCL: a parallel programming standard for heterogeneous computing systems, *IEEE Des. Test* 12 (3) (2010) 66–73.
- [27] L. Shepp, B.F. Logan, The Fourier reconstruction of a head section, *IEEE Trans. Nucl. Sci.* 3 (NS-21) (1974) 21–43.
- [28] J.R. Kremer, D.N. Mastronarde, J.R. McIntosh, Computer visualization of three-dimensional image data using IMOD, *J. Struct. Biol.* 116 (1) (1996) 71–76.
- [29] D. Salomon, *Data Compression: The Complete Reference*, Springer Science & Business Media, 2007.
- [30] C. Wang, Q. Xiangchen, Y. Yong, D. Feng, W. Huaxiang, An evaluation method for reconstructed images in electrical tomography, *FMTC*, 2008.
- [31] Z. Wang, A.C. Bovik, H.R. Sheikh, E.P. Simoncelli, Image quality assessment: From error visibility to structural similarity, *IEEE Trans. Image Process.* 13 (4) (2004) 600–612.
- [32] T. Dahmen, L. Marsalek, N. Marniok, B. Turoňová, S. Bogachev, P. Trampert, S. Nickels, P. Slusallek, The Ettention software package, *Ultramicroscopy* 161 (February) (2016) 110–118.
- [33] T. Dahmen, P. Trampert, J. Weickert, and P. Slusallek, Space-filling curve indices as acceleration structure for exemplar-based inpainting *arXiv Prepr. 1712.06326*, December 2017.